



# Engineered nanoconfinement activates Fenton catalyst at neutral pH: Mechanism and kinetics study

Jianfeng Zheng<sup>a</sup>, Yichuan Li<sup>b</sup>, Shuo Zhang<sup>c,\*</sup>

<sup>a</sup> Tianjin Key Laboratory of Aquatic Science and Technology, School of Environmental and Municipal Engineering, Tianjin Chengjian University, Jinjing Road 26, Tianjin 300384, PR China

<sup>b</sup> China Water Resources Beifang Investigation, Design and Research Co. Ltd, Tianjin 300222, PR China

<sup>c</sup> MOE Key Laboratory of Pollution Processes and Environmental Criteria, College of Environmental Science and Engineering, Nankai University, Tongyan Road 38, Tianjin 300350, PR China

## ARTICLE INFO

### Keywords:

Fenton catalyst  
Nanoconfinement  
Activation  
Protonation  
Neutral pH

## ABSTRACT

We proposed to establish nanoscale spatially confined Fenton treatment architectures to overcome the catalyst deactivation issue frequently seen at neutral pH. We demonstrated this idea by growing four typical iron oxide catalysts ( $\text{Fe}_3\text{O}_4$ ,  $\text{FeOOH}$ ,  $\text{CuFe}_2\text{O}_4$ , and  $\text{FeOCl}$ ), respectively inside the nanochannels of anodized aluminum oxide scaffold, wherein the confined space ( $\approx 5$  nm) significantly accelerated heterogeneous Fenton treatment of organic pollutants, with up to 310 times kinetics enhancement under normalized surface area compared to the counterpart bulk reactions with suspension catalysts. Based on experimental and computational studies, we gained the mechanistic details on how did the nanoconfinement enhanced the protonation of surfaces driving the catalysis, and showed how much of its significance over other influencing factors on enhancing the treatment kinetics and a sustained catalysis. Our findings mark an important advance on developing nanoconfined Fenton treatment systems that enable efficient catalyst activation and maximal treatment kinetics, without additional chemicals or electro-/photo-energies.

## 1. Introduction

Heterogeneous Fenton reaction is a promising advanced oxidation treatment technology capable to remove nonbiodegradable and toxic organic micropollutants in industrial wastewaters. With solidified iron as the catalyst, it offers rapid production of hydroxyl radical ( $\bullet\text{OH}$ ) in a way similar to the standard Fenton reaction ( $\text{Fe(II)} + \text{H}_2\text{O}_2 + \text{H}^+ \rightarrow \text{Fe(III)} + \bullet\text{OH} + \text{H}_2\text{O}$ ), together with the merits of simple operation, low cost, and absence of sludge compared to homogeneous Fenton systems. While iron sites (especially the  $\text{Fe(III)}$ ) tend to be hydroxylated in non-acidic conditions that causes the loss of catalyst activity for  $\text{H}_2\text{O}_2$  activation, the involvement of sufficient protons ( $\text{H}^+$ ) at surface region is of great importance to keep the iron sites freshly available for catalysis as well as to keep running of cycled catalytic reactions. Unfortunately, most Fenton catalysts have shown workable pHs no more than 5 without assistant chemicals [1], far from ideal for the treatment of industrial wastewaters with pHs normally ranging from 6 to 8.

Great efforts have been made so far to overcome the catalyst deactivation issue. A typical strategy is to change the iron coordination

structure, through the production of oxygen vacancies [2], instable ligands like the  $\text{Fe-Cl}$  bond [3], single-atom iron [4], and iron oxide species with other metal dopants (e.g., Ce [5], Cu [6], and Mn [7]). Relevant methods have made catalysts less pH-sensitive and more reactive, but still cannot solve the problem of catalyst deactivation at neutral or near-neutral conditions with severe shortage of protons [1,4,8,9]. Other workable methods include the addition of assistant chemicals (e.g., organic chelators to maintain the iron sites in a soluble state [10]), or exertion of external energies (e.g., electrochemical treatment [11], photo-irradiation [12], and microwave [13]), which are cost burden and may have secondary pollution risks. For the pros and cons, engineered applications have consumed great amount of acid and sometimes iron salts to the reaction units to maintain an expected and sustained treatment effect, which greatly enhanced the operation cost and have iron sludge problems.

The discoveries in diverse fields have shown that the reduction of reaction space down to nanoscale can reduce local pH, since the spatial confinement can greatly change the dynamics and dissociation of water molecules [14] as well as the electrostatic absorption of protons on

\* Corresponding author.

E-mail address: [shuo.zhang@nankai.edu.cn](mailto:shuo.zhang@nankai.edu.cn) (S. Zhang).

<https://doi.org/10.1016/j.apcatb.2023.123555>

Received 29 August 2023; Received in revised form 9 November 2023; Accepted 22 November 2023

Available online 25 November 2023

0926-3373/© 2023 Elsevier B.V. All rights reserved.

charged surfaces in nanopores or nanochannels [15]. The protonation enhancement effect has been unveiled by an electron paramagnetic resonance technology, where the pH in a 18 nm nanopore reduced almost 1 unit compared to the bulk solution [16]. Also, it has been indicated that the activity of protons is tunable and can be enhanced under nanoconfinement, especially for those nanopores less than 5 nm [17–19]. For example, the proton transport across a silica nanochannel ( $\approx 2.3$  nm diameter) enhance at least 4 times compared to that in aqueous bulk phase [19]. Overall, the enhancement of protonation have been discovered in various systems as can potentially serve for diverse fields, like in Pt-Ni nanoparticles for enzyme mimics [17], Pt oxide nanopores for fuel cell [18], silica nanochannels for biological synthesis [19], and confined  $\text{Mn}_3\text{O}_4$  for spontaneous pollutant remediation [20].

Here, we for the first time show the feasibility of nanoconfinement control as an approach to activate Fenton catalyst at neutral pH. We proved this idea by loading iron oxide catalyst nanoparticles (i.e.,  $\text{Fe}_3\text{O}_4$ ,  $\text{FeOOH}$ ,  $\text{CuFe}_2\text{O}_4$ , and  $\text{FeOCl}$ , respectively) inside the nanochannels of anodized aluminum oxide and conducting flow-through treatment tests on the nanoreactors. We unveiled the catalyst activation effect inside the nanoreactors in terms of the treatment kinetics modeling and radical production, and further obtained the mechanistic details on how did the protonation at catalyst surfaces get enhanced under nanoconfinement, based on the experimental data and computational study. While the catalyst activation effect revealed here can perfectly combine with another merit of confinement that enhances instantaneous  $\bullet\text{OH}$  exposure [21–23], we underscore the unique merit of nanoconfinement architectures on heterogeneous Fenton treatment, in which the short-lived  $\bullet\text{OH}$  not only maximally produced at neutral condition but synchronously maximally utilized for organic pollutant degradation. We further show the great feasibility of using engineered nanoreactors on the abatement of organic pollution from industrial wastewater backgrounds. Our study highlights the nanoconfinement control can be explored as a technical tool to boost heterogeneous Fenton treatment technology for practical applications.

## 2. Materials and methods

### 2.1. Materials and reagents

Anodized aluminum oxide (AAO) templates (double-pass; thickness, 60  $\mu\text{m}$ ; diameter, 2.4 cm; composition,  $\beta\text{-Al}_2\text{O}_3$ ) with different pore sizes (less than 20 nm, 40–70 nm, and 200–300 nm, respectively) were purchased from Pu-Yuan Nano Technology Co., Ltd. (Hefei, China). All the chemicals used for catalyst synthesis and reaction tests were purchased from Sigma-Aldrich and used as received without further purification.

### 2.2. Characterizations

Nanoreactor morphologies were examined by scanning electron microscopy (SEM) with a Hitachi SU-70 analytical field emission microscope (accelerating voltage = 5 kV). X-ray diffraction (XRD) patterns were obtained using a Rigaku SmartLab X-ray diffractometer (Cu K $\alpha$  monochromatic radiation operated at 40 kV and 44 mA). The Brunauer–Emmett–Teller specific surface areas ( $S_{\text{BET}}$ ) were calculated based on the nitrogen adsorption-desorption isotherms detected at  $-196.15^\circ\text{C}$  with Autosorb-iQ-C (Quantachrome, USA). Electron paramagnetic resonance (EPR) tests were performed by a Bruker A200 spectrometer (Germany). The settings: center field, 3350 G; sweep width, 200 G; static field, 3250 G; microwave bridge frequency, 9.43 GHz; power, 2.11 mW; modulation frequency, 100 kHz; modulation amplitude, 2.00 G; conversion time, 40 msec.

High-performance liquid chromatography (HPLC, Agilent Technologies 1260 Infinity) was employed for detecting organic concentration, and the stationary phase was a 5  $\mu\text{m}$  Eclipse XDB-C18 column (4.6 mm  $\times$  150 mm). Bisphenol A (BPA) was detected at 230 nm with the mobile phase of acetonitrile (50%) and 0.1% phosphoric acid solution (50%)

under a flow rate of 1.0 mL min $^{-1}$ . *Para*-chlorobenzoic acid (pCBA) was detected at 237 nm with the mobile phase of acetonitrile (50%) and 0.1% phosphoric acid solution (50%) under a flow rate of 1.5 mL min $^{-1}$ . Aniline was detected at 230 nm with the mobile phase of acetonitrile (60%) and 0.1% phosphoric acid solution (40%) under a flow rate of 1.0 mL min $^{-1}$ . Acetaminophen was detected at 244 nm with the mobile phase of methanol (35%) and 0.05% trifluoroacetic acid solution (65%) under a flow rate of 1.0 mL min $^{-1}$ . The solutions for 4-nitrophenol and methylene blue (MB) were examined by a 756-PC UV/Vis spectrometer (Shanghai Spectrum Instruments Co., Ltd., China), and the concentration of MB was determined at wavelength of 664 nm according to the Lambert-Beer's law. The total organic carbon (TOC) was determined using a Shimadzu TOC-VCSH analyzer.

### 2.3. Batch reaction tests

Prior to catalyst testing, a 100 mL stock solution containing both the  $\text{H}_2\text{O}_2$  and BPA was prepared under a buffered solution pH (20 mM phosphate). The catalyst powders were first ultrasonically dispersed in an aliquot of ultrapure water (2% volume of the stock solution) and then transferred to the stock solution to initiate the heterogeneous Fenton reaction. Except for  $\text{Fe}_3\text{O}_4$ , the batch reactor was magnetically stirred to maintain complete mixing and turbulent conditions; for  $\text{Fe}_3\text{O}_4$ , mechanical stir was used to avoid particle aggregation at the bottom of reactor by magnetic attraction (illustrated in Fig. S1a). As reactions proceeded, samples were periodically withdrawn at predetermined time intervals, centrifuged to remove the solid phase, and immediately sent to HPLC analysis. All the experiments were performed at room temperature.

### 2.4. Nanoreactor tests

Catalytic reactions inside the AAO-templated nanoreactors were performed with a filtration setup illustrated in Fig. S1b. Briefly, the membrane material was placed on top of a perforated glass support, upon which a concentrically shaped rubber pad was fixed to control the effective flow-through area as well as to avoid any liquid leakage. The test solution containing  $\text{H}_2\text{O}_2$  and model organics was injected from a syringe into the sealed reactor at a fixed flow rate driven by a micro-pump. The pH was controlled by a 20 mM phosphate buffer solution. The permeate samples after reaction were collected and immediately sent for analysis (HPLC, EPR, UV-Vis, etc.). All the experiments were performed at room temperature.

### 2.5. Computational method and model

Molecular dynamics (MD) simulations were performed using the Forcite module in the Materials studio package. The module consists of two slabs used for the spatial confinement with configurations obtained from Materials Project. Specifically,  $\text{Fe}_3\text{O}_4$  (311)- $\text{Al}_2\text{O}_3$ (002) slab with 34.63 Å  $\times$  34.63 Å area,  $\text{FeOOH}$  (020)- $\text{Al}_2\text{O}_3$ (002) slab with 36.32 Å  $\times$  35.75 Å area,  $\text{CuFe}_2\text{O}_4$  (311)- $\text{Al}_2\text{O}_3$ (002) slab with 34.50 Å  $\times$  34.50 Å area, and  $\text{FeOCl}$  (010)- $\text{Al}_2\text{O}_3$ (002) slab with 35.77 Å  $\times$  35.06 Å area. The background water phase containing sufficient number of protons (presented as hydronium ions,  $\text{H}_3\text{O}^+$ ) was set between the slabs to counterbalance the electric charge on catalyst surfaces, and the overall system had a fully hydrated interface and was kept in electroneutrality. The system under went energy minimization and then Canonical simulations were performed for 1 ns with an Andersen thermostat. COM-PASSII force field was selected to represent the interaction between microscopic particles. We chose a 1 fs time step to ensure the stability of bonded interactions and employed the Ewald method for the correction of long-range electrostatic interactions.

### 3. Results and discussion

#### 3.1. Deactivation of Fenton catalyst at neutral pH

Iron oxide species with solidified Fe-sites can trigger the Haber-Weiss cycle that transforms  $\text{H}_2\text{O}_2$  to  $\bullet\text{OH}$  at the surface [24]. This was demonstrated by four typical iron oxide catalysts (i.e.,  $\text{Fe}_3\text{O}_4$ ,  $\gamma\text{-FeOOH}$ ,  $\text{CuFe}_2\text{O}_4$ , and  $\text{FeOCl}$ ; Text S1 for synthetic details; Fig. S2 for XRD patterns), respectively in reaction with  $\text{H}_2\text{O}_2$  at varying solution pH (Fig. 1). Bisphenol A (BPA) was employed as the radical indicator as it is very sensitive to  $\bullet\text{OH}$  attack ( $k_{\text{OH/BPA}} \approx 6.9 \times 10^9$  [25]) but almost unreactive to  $\text{H}_2\text{O}_2$  (Fig. S3). All the reaction systems caused gradual disappearance of BPA within the tested pH window of 3.0–7.0 (Fig. 1a–e). While the adsorption effect was negligible for the solid phase (Fig. S4a), the organic removal indicates an occurrence of heterogeneous Fenton reaction with continuous production of  $\bullet\text{OH}$ . All the BPA degradation processes followed pseudo-first order kinetics with the rate constants shown in Fig. 1f ( $R^2 = 0.986\text{--}0.996$ ).

The four catalysts exhibited differed activity ( $\text{FeOCl} > \text{CuFe}_2\text{O}_4 > \gamma\text{-FeOOH} > \text{Fe}_3\text{O}_4$ ) because different coordination structure of iron has different  $\text{H}_2\text{O}_2$  binding and activation behavior. The best catalytic performance of  $\text{FeOCl}$  is due to the unsaturated iron sites weakly bond to chloride and energetically favorable Fe(III)-to-Fe(II) reduction in reaction with  $\text{H}_2\text{O}_2$  [3,26,27]. Notably, for all the catalysts, the increment of pH caused a sharp reduction of catalytic activity, especially when the pH was more than 5.0 (Fig. 1f). When the pH reached 7.0, all the four catalysts became almost totally deactivated. Even for the outstanding  $\text{FeOCl}$  structure, the rate constant reduced 226 times from  $7.2 \times 10^{-2} \text{ min}^{-1}$  at pH 3.0 to about  $3.2 \times 10^{-4} \text{ min}^{-1}$  at pH 7.0. Similar trends for the pH reliance have been reported in the past works with either modified iron structures or single-atom iron that were reactive at acidic conditions but became significantly deactivated with a shortage of

protons at neutral or near-neutral pH conditions [1,4,8,9].

#### 3.2. Kinetics enhancement under spatial confinement

In contrast to the traditional ways of adding acid chemicals or external electro-/photo-energies for the catalyst activation, we here introduce an innovative approach to keep Fenton catalyst highly activated at neutral pH simply through engineering nanoconfinement architectures. We choose anodized aluminum oxide (AAO) as the template with uniform and aligned channels (Fig. S5) and synthesized iron oxide nanoparticles alongside the inner wall of AAO (Text S2 for synthetic methods; Fig. 2a for the SEM results). The XRD results (Fig. 2b) show that the as-synthesized iron oxide nanoparticles inside the AAO were chemically consistent with the iron oxide particles used in the above-discussed batch study. The iron oxide nanoparticles grown in AAO were controlled at about 15 nm in diameter, so that the pore sizes for confinement control were about 5 nm for all the catalysts. While the top faces of the membranes were polished (Fig. S6; Text S2 for polishing methods), all the catalytic reactions can be strictly controlled inside the nanochannels. Thus, as each channel can be taken as a nanoreactor, the AAO-catalyst composite materials were labeled as “NR-x”, where the “x” indicates a specific iron oxide species (e.g., NR- $\text{Fe}_3\text{O}_4$  denotes the nanoreactors containing  $\text{Fe}_3\text{O}_4$  nanoparticles).

The spatially confined heterogeneous Fenton reactions were triggered by pushing BPA and  $\text{H}_2\text{O}_2$  mixture solution through the membrane with aligned nanoreactors (Fig. S1b). As shown in Fig. 3a, all the four kinds of NRs achieved complete BPA removal within the retention times of less than 10 s. The fast removal of BPA by the NRs is in marked contrast to the batch reaction systems with extremely slow removal at neutral pH (less than 10% after 2.5 h treatment, Fig. 1e). For the NRs, the retention time ( $R_t$ ) reversely correlates to water flux ( $Q$ ) ( $R_t = V_p/Q$ ,  $V_p$  is the pore volume inside NRs; Table S1 for details) that was driven by

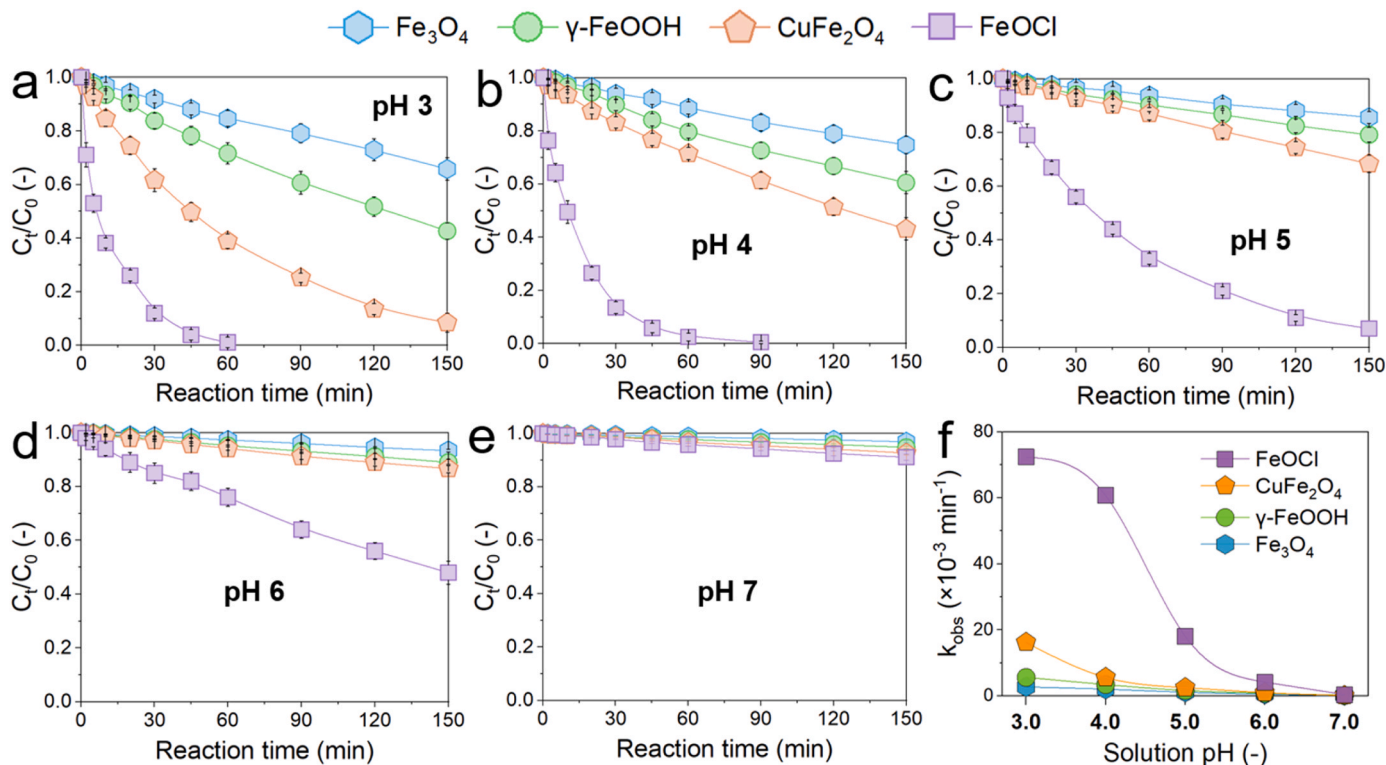


**Fig. 1.** Evolution of normalized BPA concentration during batch-mode heterogeneous Fenton treatment with different iron oxide catalysts under the solution pHs of (a) 3.0, (b) 4.0, (c) 5.0, (d) 6.0, and (e) 7.0, respectively. The first sample for the starting point “ $C_0$ ” was immediately detected after the addition of solid, so as to minimize any possible interferences in the kinetics analysis. (f) Evolution of the pseudo-first-order rate constant ( $k_{\text{obs}}$ ) as a function of solution pH for different iron oxide catalysts. Conditions: solid load, 0.1 g  $\text{L}^{-1}$ ; initial BPA concentration, 20  $\mu\text{M}$ ; initial  $\text{H}_2\text{O}_2$  concentration, 2 mM. All the error bars represent the data from triplicated tests.



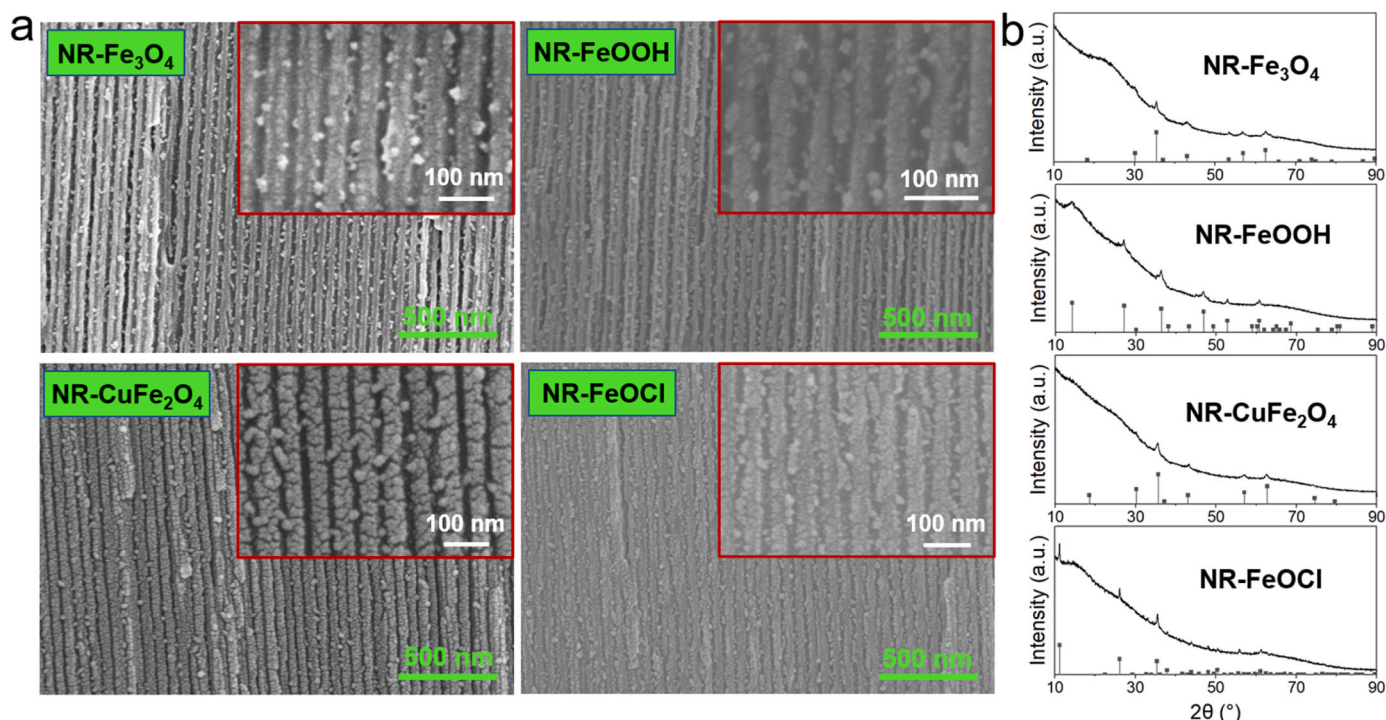


**Fig. 2.** (a) Cross-sectional SEM images of NR-Fe<sub>3</sub>O<sub>4</sub>, NR-FeOOH, NR-CuFe<sub>2</sub>O<sub>4</sub>, and NR-FeOCl, respectively. Inset figure is the magnified cross-sectional SEM images. (b) The XRD patterns of NR-Fe<sub>3</sub>O<sub>4</sub> (reference PDF#19-0629), NR-FeOOH (reference PDF#08-0098), NR-CuFe<sub>2</sub>O<sub>4</sub> (reference PDF#25-0283), and NR-FeOCl (reference PDF#72-0619), respectively.

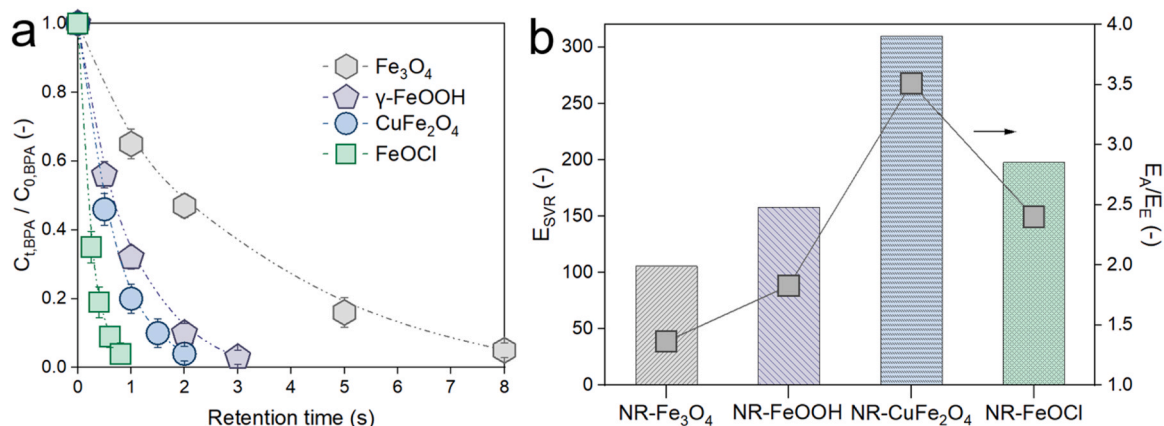


**Fig. 3.** (a) Evolution of normalized BPA concentration *versus* retention time as a function of the confined heterogeneous Fenton reaction in different NRs systems. Conditions: entrance organic concentration, 20  $\mu$ M; entrance H<sub>2</sub>O<sub>2</sub> concentration, 2 mM; solution pH, 7.0. All the error bars represent the data from triplicated tests. (b) The enhancement factor ( $E_{SVR}$ ) and relative enhancement effect ( $E_A/E_E$ ) for NR-Fe<sub>3</sub>O<sub>4</sub>, NR-FeOOH, NR-CuFe<sub>2</sub>O<sub>4</sub>, and NR-FeOCl, respectively, compared to the batch-mode reactions with suspension catalysts.

the transmembrane pressure (Fig. S7 for details). Note that BPA adsorption by the NRs was negligible (Fig. S4b), we obtained the confined Fenton treatment kinetics constants according to the linear regression analysis (Fig. S8), based on the fact that a reduced retention time inside the NRs conceptually equals a shortened reaction in a batch reactor. Results show that the NRs significantly enhanced the rate constants for pollutant degradation (data listed in Table S1) compared to the counterpart batch reaction systems (data listed in Table S2); specifically,  $2.1 \times 10^5$  times enhancement for NR-Fe<sub>3</sub>O<sub>4</sub>,  $6.4 \times 10^5$  times enhancement for NR-FeOOH,  $7.6 \times 10^5$  times enhancement for NR-CuFe<sub>2</sub>O<sub>4</sub>, and  $8.3 \times 10^5$  times enhancement for NR-FeOCl.

Meanwhile,  $\bullet$ OH signal inside the NRs can be detected with EPR analysis performed using 5,5-dimethylpyrroline-oxide (DMPO) as a

spin-trapping agent ( $k_{\bullet\text{OH}/\text{DMPO}} \approx 3.4 \times 10^9 \text{ M}^{-1} \text{ s}^{-1}$  [28]). As shown in Fig. 4, all the signals for  $\bullet$ OH confined inside the NRs were much stronger than those obtained from the batch reaction with a high concentration of catalyst suspension (5 g L<sup>-1</sup>), which indicates a relatively huge amount of  $\bullet$ OH had been produced instantaneously inside the NRs. The intensity of EPR signal roughly followed the order of NR-FeOCl > NR-CuFe<sub>2</sub>O<sub>4</sub> > NR-FeOOH > NR-Fe<sub>3</sub>O<sub>4</sub>, consistent with the order of kinetics constants obtained for BPA degradation (Fig. 3a). The highly efficient production of  $\bullet$ OH is also reflected by the fast generation of hydroxyterephthalate (hTPA) after the injection of terephthalic acid (TPA) as a  $\bullet$ OH probe ( $k_{\bullet\text{OH}/\text{TPA}} \approx 4.4 \times 10^9$  [29]) (Fig. S9). For the batch reactions, in contrast, the increment of hTPA concentration took about 20 h to get a maximal value (Fig. S10). Also, the internal reactions were

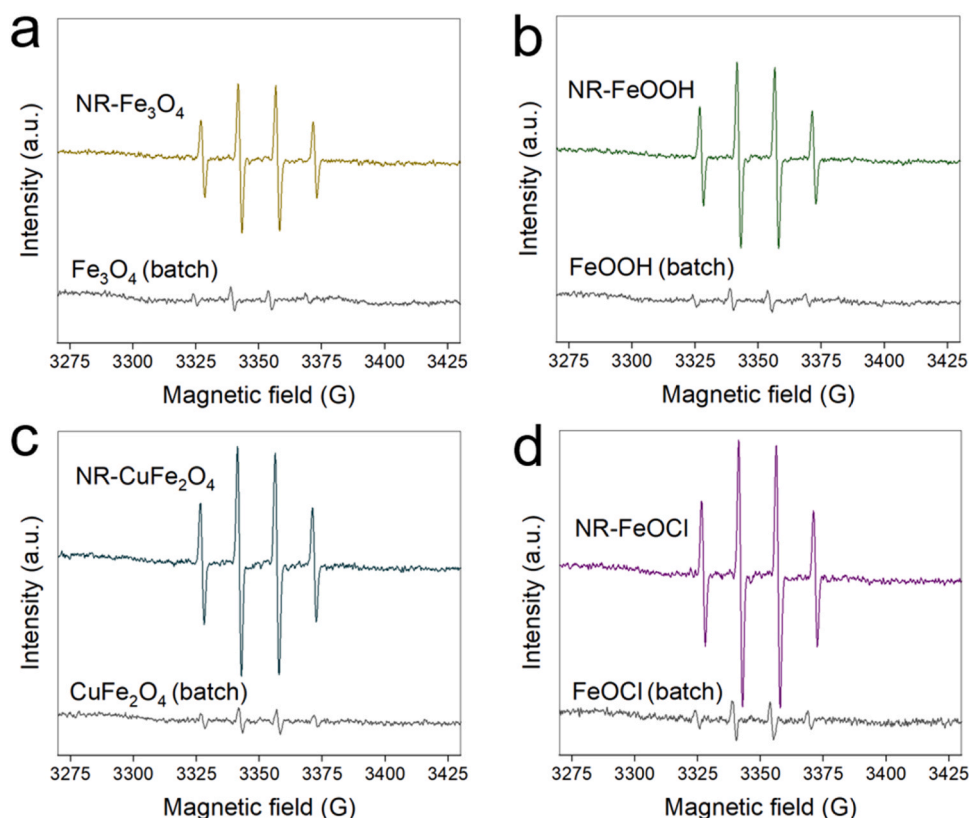


**Fig. 4.** EPR spectra of the DMPO spin-trapping for the heterogeneous Fenton reactions occurred inside the NRs and batch reactors, respectively. Conditions: DMPO concentration, 0.2 mM; solution pH, 7.0; solid catalyst load in batch reactor: 5 g L<sup>-1</sup>; retention time for the NRs test, 5 s. The peaks emerged are DMPO-OH ( $a_N = a_H = 14.9$  G).

completely inhibited with the addition of *tert*-butanol alcohol (TBA) as a  $\bullet$ OH quencher ( $k_{TBA/\bullet OH} = 6 \times 10^8 \text{ M}^{-1} \text{ s}^{-1}$  [30]; Fig. S11), showing the dominant role of  $\bullet$ OH for the organic pollutant removal. Together with radical production, the precursor  $\text{H}_2\text{O}_2$  was consumed inside the NRs whose concentration decreased in the effluents, and the concentration reduction was more obvious for the NRs with a relatively stronger catalyst (Fig. S12). All the results indicate the occurrence of highly efficient heterogeneous Fenton reaction inside the NRs. Also, it should be clarified that we have employed an optimal concentration of  $\text{H}_2\text{O}_2$  for the NRs tests (*i.e.*, 2 mM), since a higher amount of  $\text{H}_2\text{O}_2$ , especially for those over 5 mM, had caused a kinetically considerable quenching of  $\bullet$ OH and led to a reduction of the treatment kinetics (Fig. S13).

Note that the available surface area for the catalytic reaction is different between the NRs and the batch reactor. We normalized the surface-to-volume ratio (SVR) to obtain the kinetics enhancement factor ( $E_{SVR}$ ; Text S3 for calculation details and Fig. S14 for surface area analysis), so that any difference in the SVR-normalized reactivity can be related to the spatial confinement effect. Under spatial confinement, all the four catalysts in the NRs seemed to be “activated” with more than two orders of magnitude kinetics enhancement under normalized surfaces compared to that without confinement (Fig. 3b). It has been recognized that spatial confinement can enhance the exposure of  $\bullet$ OH product [21,23] that has extremely short lifetime in aqueous bulk ( $<10 \mu\text{s}$  [31]). Such a positive effect for radical exposure enhancement (labeled as “ $E_E$ ”) can be roughly estimated by the  $E_{SVR}$  at pH 3.0 where the protonation is sufficient for radical production and the  $\bullet$ OH mass transfer is the rate-limiting factor for a specific catalyst. While the radical exposure is sensitive to the size of confinement, our obtained values of  $E_E$  almost stay at a same level within the range of 8–10 (Fig. S15 for details), due to the quite similar extent of spatial nanoconfinement among our tested NRs ( $\approx 5$  nm; Fig. 2a).

When the solution pH came to 7.0, the  $E_{SVR}$  values for the four NRs

significantly enhanced compared to that for pH 3.0; specifically, about 106 for NR- $\text{Fe}_3\text{O}_4$ , 158 for NR- $\text{FeOOH}$ , 310 for NR- $\text{CuFe}_2\text{O}_4$ , and 198 for NR- $\text{FeOCl}$  (Fig. 3b). Such an obvious higher  $E_{SVR}$  at pH 7.0 indicates that the spatial confinement was not just limited to the control of  $\bullet$ OH exposure, but had more likely elevated the catalysts’ activity toward  $\bullet$ OH production (we will show the mechanistic details for the protonation enhancement effect in the next section). We termed this catalyst activation effect under nanoconfinement as “ $E_A$ ”. With the consideration that the enhanced gross kinetics (*i.e.*,  $E_{SVR}$ ) correlate proportionally to the extent of the enhanced  $\bullet$ OH production (*i.e.*,  $E_A$ ) as well as the enhanced  $\bullet$ OH exposure (*i.e.*,  $E_E$ ), the NRs-based kinetics enhancement can be quantified with the formula “ $E_{SVR} = E_A \times E_E$ ”.

It should note that, for neutral pH condition, the confinement-based catalyst activation became of even higher importance than that for  $\bullet$ OH exposure enhancement, not only because that the former was relatively higher than the latter ( $E_A/E_E > 1$ , Fig. 3b), but the fact that all the catalysts were extremely weak on reaction without a confinement control (Fig. 1f). We also recorded the greatly differed “ $E_A/E_E$ ” values among the NRs with different catalysts, which implied that the surface protonation effect may be further modulated by the chemical structure of catalyst if properly designed under nanoconfinement. Relevant observations stimulated our further study to gain more evidences and mechanistic insights about how nanoconfinement was at play to control the surface protonation so as to keep the catalysts highly activated.

### 3.3. Mechanisms of the nanoconfinement effect

The above study has shown that our tested Fenton catalysts were inert at neutral pH when used as suspensions, but became active when confined in the nanoreactors. Such a great difference aroused our speculation that the confined geometry might have changed the protonation behaviors at catalyst surfaces. Previous studies have

demonstrated that the spatial confinement overlaps the electrical double layers of charged surfaces and therefore increases the electrical potential inside nanopores [15]. As a result, the electrostatic interactions between negatively charged iron oxide surfaces and protons inside nanopores might have been improved, causing enhanced concentration of protons inside the pores compared to the bulk solution. The enhanced protonation can be evidenced by the shift of the UV-Vis absorption peak for 4-nitrophenol solution [32–34] before and after it went through the nanochannels of NR-CuFe<sub>2</sub>O<sub>4</sub>, as well as the observable color change from yellow (pH 7.0) to light yellow for the permeate solution (Fig. S16 for detailed discussion).

To quantify the average pHs inside the pores of the NRs (i.e., pH<sub>pore</sub>), we employed a model based on the mean-field Donnan theory (calculation details in Text S4). As shown in Fig. 5a, the spatial confinement at nanoscale can lead to a reduction of the pH<sub>pore</sub>, and the difference of the pH<sub>pore</sub> from bulk pH closely correlate with the charge property of Fenton catalyst. Specifically, while CuFe<sub>2</sub>O<sub>4</sub> has the highest charge density ( $\sigma_{\text{CuFe}_2\text{O}_4}=0.57 \text{ C m}^{-2}$ ; obtained by Python) than other catalysts ( $\sigma_{\text{Fe}_3\text{O}_4}=0.54 \text{ C m}^{-2}$ ;  $\sigma_{\text{FeOOH}}=0.47 \text{ C m}^{-2}$ ;  $\sigma_{\text{FeOCl}}=0.32 \text{ C m}^{-2}$ ), it showed the lowest average pH<sub>pore</sub> that dropped from bulk pH of 7.0 to about 4.9, more than 2 units. As a result, the E<sub>A</sub> for NR-CuFe<sub>2</sub>O<sub>4</sub> reached up to 33, with the enhancement of kinetics constant almost equivalent to that for the batch reactions with solution pH adjusted from 7.0 ( $2.3 \times 10^{-6} \text{ s}^{-1}$ ) down to 4.0 ( $9.3 \times 10^{-5} \text{ s}^{-1}$ ) (ca. 40 times enhancement, Fig. 1). The in-pore protonation enhancement can well explain our recorded catalyst activation effect on both the treatment kinetics and radical production.

Our previous work [21] had shown that the size of confinement should at least below 20 nm to keep a maximal •OH exposure (i.e., E<sub>E</sub>); otherwise, reactions in a larger space would suffer from a significant loss of radicals. So, further reducing the nanopore size below 20 nm would bring a dual effect on the treatment kinetics enhancement ( $E_A \times E_E$  decides how much benefits can be eventually taken from the nanoconfinement control). In other words, one cannot benefit much from larger pores. As examples, if we extend the pore size of NR-CuFe<sub>2</sub>O<sub>4</sub> to about 30 nm (Fig. S17a), the E<sub>SVR</sub> reduced to about 44 (Fig. 5b), with only a partial contribution of the E<sub>A</sub> and E<sub>E</sub>; if we extend the pore size of NR-CuFe<sub>2</sub>O<sub>4</sub> to 200–300 nm (Fig. S17b), the confinement effect almost disappeared ( $E_{\text{SVR}} \approx 1$ ; Fig. 5b), due to the negligible confinement effect on both the protonation and radical transfer.

While a reduction of pore size below 10 nm will not add much to •OH transfer enhancement [21], we noticed that the E<sub>SVR</sub> for BPA degradation further enhanced when the confined space reduced from 10 nm ( $E_{\text{SVR}}=207$ ; details in Fig. S18a) to 5 nm ( $E_{\text{SVR}}=310$ ; Fig. 5b). Such a great difference implied a further intensified protonation effect

on the catalyst activation. Nanoconfinement has been shown to hinder the localized screening effect of counterions at surfaces, leading to preferred binding of counterions to surfaces and a shift of their equilibrium distribution [35]. With the MD simulation, we revealed the spatial heterogeneity of protons under nanoconfinement. The results of the simulation suggested that the H<sub>3</sub>O<sup>+</sup> concentration would be much higher near the surface of catalyst than the average in-pore H<sub>3</sub>O<sup>+</sup> concentration (Fig. 6). The enriched protons at surface region further contributes to the enhanced kinetics for heterogeneous Fenton treatment. Similar simulation results have been reported with pore sizes generally less than 5 nm for different materials such as silica [35], manganese [20], nickel [17], and platinum [18]. In contrast, when we increased the channel size from 5 to 15 nm, the heterogeneous state of H<sub>3</sub>O<sup>+</sup> was largely lessened (Fig. S19). Moreover, the activity of protons might be simultaneously enhanced when confined at nanoscale below 5 nm [17–19], e.g., the activity of H<sup>+</sup> inside silica nanopores (about 2.3 nm diameter) enhanced at least 4 times compared to the counterpart H<sup>+</sup> at outer space [19]. Although we do not have experimental evidence, this is in agreement with our observed kinetics results that when the pore size of NR-CuFe<sub>2</sub>O<sub>4</sub> further reduced to about 3 nm (Fig. S18b), the E<sub>A</sub> was further enhanced (Fig. 5b). That is to say, the protonation enhancement effect is still tunable even for the confined space reduced down to several nanometers.

Consequently, due to the nanopore absorption of protons as well as their enhanced activity, the kinetics of heterogeneous Fenton reaction inside the NRs was totally different from that in bulk solution. It should be emphasized that, the •OH production enhancement not only correlates with the extent of protonation but with the intrinsic ability of catalyst on H<sub>2</sub>O<sub>2</sub> activation. For example, the pronation effect for FeOCl is weaker compared to Fe<sub>3</sub>O<sub>4</sub> and γ-FeOOH (Figs. 5 and 6), but the E<sub>A</sub> for FeOCl is higher than both of them (Fig. 3b). This is because that, while FeOCl is more sensitive in catalysis than other iron catalysts, more benefits have been taken from the protonation effect with a more efficient H<sub>2</sub>O<sub>2</sub>-to-•OH transformation. In contrast to Fe<sub>3</sub>O<sub>4</sub> and γ-FeOOH, CuFe<sub>2</sub>O<sub>4</sub> not only induced stronger protonation within the nanoreactor but also was more reactive on H<sub>2</sub>O<sub>2</sub> activation, and therefore it took the most benefits on the kinetics enhancement (Fig. 3b). Thus, for the nanoconfinement control, the ideal catalyst structures should have a higher surface charge density for protonation as well as a higher sensitivity for H<sub>2</sub>O<sub>2</sub> activation.

In addition to the adverse effect on the loss of catalyst activity, neutral pH would also shorten the longevity of catalyst, with the available Fe(II) or Fe(III) sites gradually occupied by hydroxyl groups against their further access to H<sub>2</sub>O<sub>2</sub>. We demonstrated this issue by loading CuFe<sub>2</sub>O<sub>4</sub> particles on top of the AAO support and perform flow-

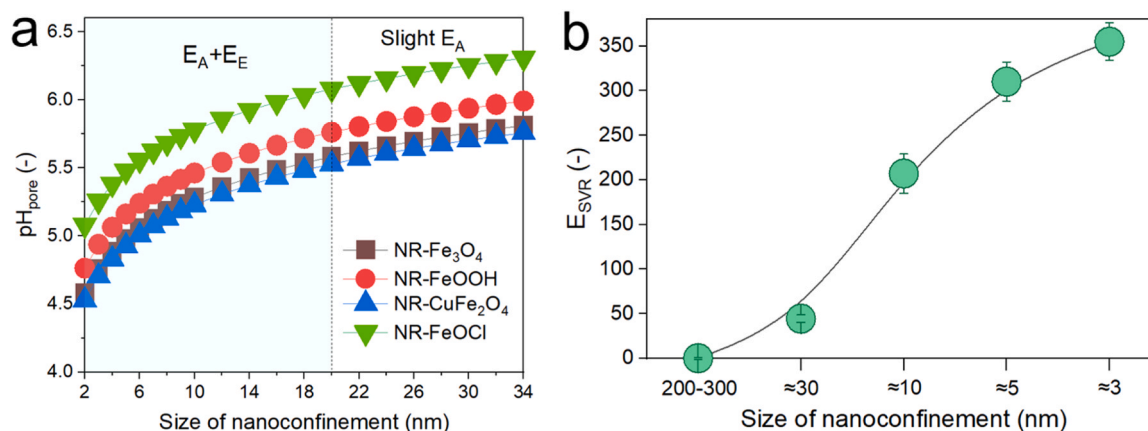


**Fig. 5.** (a) Modeled average in-pore pH (pH<sub>pore</sub>) as a function of the pore diameter for NR-Fe<sub>3</sub>O<sub>4</sub>, NR-FeOOH, NR-CuFe<sub>2</sub>O<sub>4</sub>, and NR-FeOCl, respectively. Twenty millimolar buffered solution was used as the bulk phase outside the nanopore, and the pH of the bulk solution is 7.0. (b) Evolution of E<sub>SVR</sub> as a function of the size of nanoconfinement for NR-CuFe<sub>2</sub>O<sub>4</sub>.



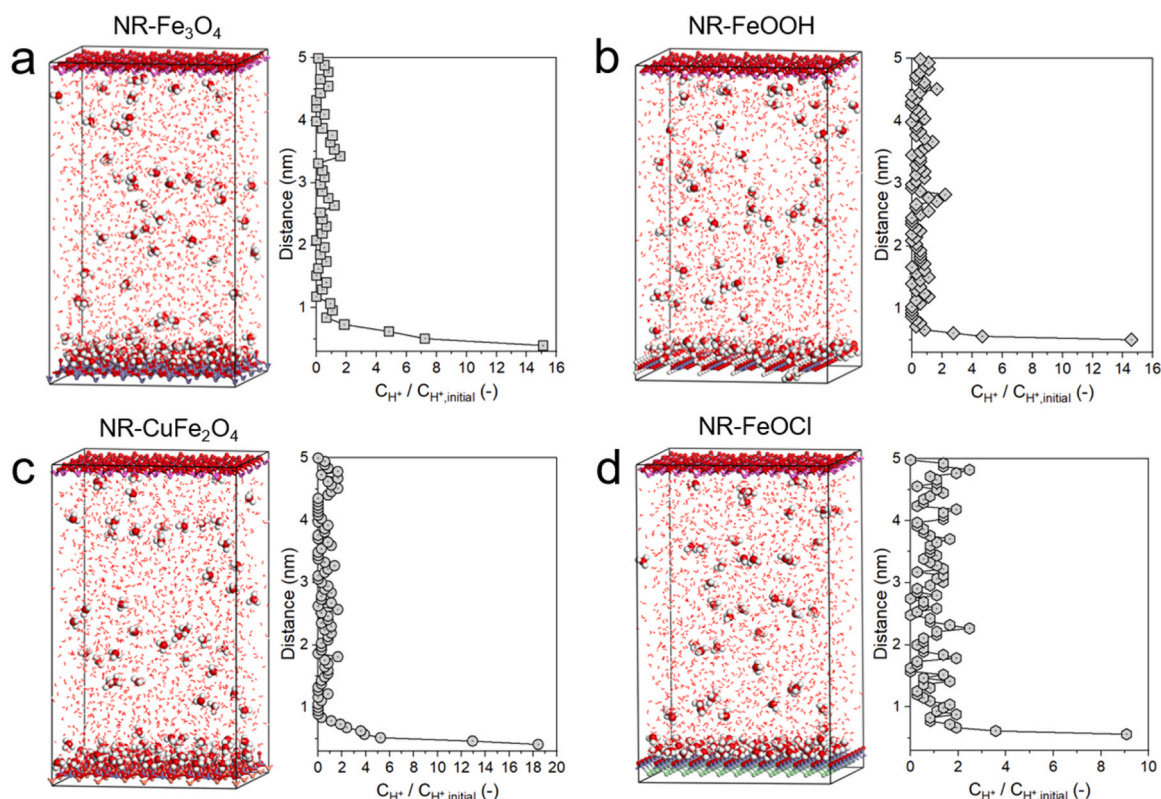


**Fig. 6.** MD simulation results of the protons distribution under nanoconfinement for (a) NR-Fe<sub>3</sub>O<sub>4</sub>, (b) NR-FeOOH, (c) NR-CuFe<sub>2</sub>O<sub>4</sub>, and (d) NR-FeOCl, respectively. The left side for each figure is the Snapshot of H<sub>3</sub>O<sup>+</sup> confined within 5 nm space between iron oxide catalysts and aluminum oxide (the cylindrical AAO channel structure was approximated by two parallel surfaces for this simulation). The number of H<sub>2</sub>O molecules and H<sub>3</sub>O<sup>+</sup> were, respectively, 1800 and 100 for this qualitative study. The pink sphere on the top is aluminum, the gray sphere at the bottom is iron, the yellow sphere at the bottom is copper, the green sphere at the bottom is chloride, the red sphere is oxygen, and the white sphere is hydrogen. The background water molecules are labeled as red dots to highlight the distribution of H<sub>3</sub>O<sup>+</sup>. The right side for each figure is the relative H<sub>3</sub>O<sup>+</sup> concentration *versus* the distance (catalyst surface is the start). The relative H<sub>3</sub>O<sup>+</sup> concentration ( $C_{H^+}/C_{H^+,initial}$ ) denotes the local H<sub>3</sub>O<sup>+</sup> concentration at a fixed distance from iron catalyst surface caused by nanoconfinement compared to the starting H<sub>3</sub>O<sup>+</sup> concentration set for the MD simulation.

through reaction (Fig. S20a). Results show that the reactivity of AAO-supported CuFe<sub>2</sub>O<sub>4</sub> gradually reduced to zero within about 45 min, whereas the AAO-confined CuFe<sub>2</sub>O<sub>4</sub> (*i.e.*, NR-CuFe<sub>2</sub>O<sub>4</sub>) with protonation effect maintained at least 8 h run on the organic pollutant removal without any loss of reactivity (Fig. S20b). Meanwhile, the confined CuFe<sub>2</sub>O<sub>4</sub> nanoparticles stay unchanged in both the morphology and chemical structure with negligible loss of iron (Fig. S21 with detailed discussion). The significantly improved catalyst longevity together with the great stability add more interests to the nanoconfinement control.

Further, regarding the spatial inhomogeneity of •OH inside the NRs, the reaction kinetics is related to how close of organic pollutants to the surface of catalyst where •OH is generated. This is reflected by the greatly differed kinetics between the degradation of positively charged methylene blue (MB; a cationic dye) and negatively charged *para*-chlorobenzoic acid (*p*CBA; pKa=3.98) (Fig. S22a; NR-CuFe<sub>2</sub>O<sub>4</sub> was used for this case study). Specifically, MB under the electrostatic attraction by CuFe<sub>2</sub>O<sub>4</sub> (negatively charged with zeta potential less than −25 mV when pH higher than 5.0) can be brought closer to the high •OH region near catalyst surface and therefore presented a higher kinetics than *p*CBA with electrostatic repulsion. Such a difference on the kinetically available •OH was particularly evident for the size of nanoconfinement larger than 10 nm (Fig. S22b; calculation details in Text S5). However, when the size of nanoconfinement was below 5 nm, the degradation kinetics were almost the same for MB and *p*CBA (Fig. S22b). This might be explained by the negligible electrostatic solute-surface attraction or repulsion under the size of confinement less than 5 nm [36], wherein the solute-surface interaction became dominated by charge independent forces such as the van der Waals force. Such a property of confined

treatment can be explored for a synchronous removal of cocktail organic contaminants with different charge properties in practical treatment scenarios.

We further tested NR-CuFe<sub>2</sub>O<sub>4</sub> with simulated industrial wastewaters containing effluent organic matter (EfOM) and common inorganic constituents (detailed component in Table S3). The EfOM quenches •OH ( $k_{\bullet OH/EfOM} \approx 6\text{--}14 \times 10^8 \text{ M}^{-1} \text{ s}^{-1}$  [37]) and thus hinder the oxidation treatment of coexisting organic pollutants, which is demonstrated in the batch reactions with CuFe<sub>2</sub>O<sub>4</sub> nanoparticles (Fig. S23a). Such a quenching effect was effectively avoided by the NR-CuFe<sub>2</sub>O<sub>4</sub> structure with a size exclusion of most of the EfOM (in terms of TOC; about 87% removed for the chemical wastewater and about 85% removed for the hospital wastewater). In this way, the nanoreactor with pore rejection protected the confined CuFe<sub>2</sub>O<sub>4</sub> catalysts and radical products from being exposed to the majority of EfOM, allowing them to selectively target the destruction of smaller organic pollutants that entered the nanopores. As a result, due to the combined size exclusion and confined advanced oxidation (retention time of 60 s), the TOC was greatly reduced (>80% removed for the chemical wastewater and >95% removed for the hospital wastewater; details in Fig. S23b). The near-complete removal of TOC from the simulated hospital wastewater was due to the absence of carbonates that would otherwise consume part of the radicals [38]. The results of our preliminary test feature the unique merits of the nanoreactor structure and its feasibility to be explored for engineered applications, albeit much optimization work will need to be done on both the material property and reaction kinetics control.

## 4. Conclusions

The deactivation of catalyst at neutral pH has been an issue that limits the application of heterogeneous Fenton reaction for practical treatment scenarios. Our study demonstrated an innovative approach to keep Fenton catalyst reactive through confining the catalytic reaction and treatment processes inside nanoscale pores. This nanoconfinement control enhanced the protonation of catalyst (*i.e.*, the reaction driving force), achieved simply with a transmembrane pressure, compared to conventional treatment processes relying on additional chemicals or electro-/photo-energy. With simultaneously enhanced  $\bullet\text{OH}$  production and exposure, our nanoreactors exhibited maximized treatment kinetics compared to the batch-mode reaction. We also recorded a greatly enhanced longevity of iron catalyst under the nanoconfinement, which is appealing for practical applications. Our discoveries on the catalyst activation effect at neutral pH mark a big progress of the researches on the heterogeneous Fenton technology with confined catalysts (details in Table S4).

With the recognition that the overall kinetics for  $\bullet\text{OH}$  production is related to the catalyst's intrinsic sensitivity on  $\text{H}_2\text{O}_2$  activation, we highlight that a rational design of catalyst for the nanoconfinement control should focus on the charge properties in terms of both the protonation control (details in our mechanism study) and the Fe(II/III) redox property for catalysis. Also, the nanoconfined reaction system can serve for a wider range of operation, with the platforms that can be designed either as mesoporous particles working as suspensions or packed-bed form, or as membrane reactors with catalyst grown inside nanopores or nanochannels (like the NRs in this study). While the AAO template is brittle and cannot be an option for practical application (though ideal for proof-of-concept study), we are currently working to explore state-of-the-art membrane scaffolds with both enough mechanical strength and regular channels for confined water treatment.

## CRediT authorship contribution statement

J.F. Zheng and S. Zhang designed research; J.F. Zheng synthesized the catalyst and nanoreactors; J.F. Zheng and Y.C. Li did material characterizations and performance test; J.F. Zheng, Y.C. Li, and S. Zhang contributed to the data interpretation; J.F. Zheng and S. Zhang wrote the paper. All authors discussed the results and commented on the manuscript.

## Declaration of Competing Interest

The authors declare that they have no known competing financial interests or personal relationships that could have appeared to influence the work reported in this paper.

## Data availability

Data will be made available on request.

## Acknowledgments

This study was funded by the National Natural Science Foundation of China (22376106) and the Fundamental Research Funds for the Central Universities (040-63233059).

## Appendix A. Supporting information

Supplementary data associated with this article can be found in the online version at [doi:10.1016/j.apcatb.2023.123555](https://doi.org/10.1016/j.apcatb.2023.123555).

## References

- [1] Q.Q. Cai, B.C.Y. Lee, S.L. Ong, J.Y. Hu, Fluidized-bed Fenton technologies for recalcitrant industrial wastewater treatment-recent advances, challenges and perspective, *Water Res.* 190 (2021), 116692.
- [2] H. Jin, X. Tian, Y. Nie, Z. Zhou, C. Yang, Y. Li, L. Lu, Oxygen vacancy promoted heterogeneous Fenton-like degradation of ofloxacin at pH 3.2–9.0 by Cu substituted magnetic  $\text{Fe}_3\text{O}_4/\text{FeOOH}$  nanocomposite, *Environ. Sci. Technol.* 51 (2017) 12699–12706.
- [3] X.J. Yang, X.M. Xu, J. Xu, Y.F. Han, Iron oxychloride ( $\text{FeOCl}$ ): an efficient Fenton-like catalyst for producing hydroxyl radicals in degradation of organic contaminants, *J. Am. Chem. Soc.* 135 (2013) 16058–16061.
- [4] Y. Yin, L. Shi, W. Li, X. Li, H. Wu, Z. Ao, W. Tian, S. Liu, S. Wang, H. Sun, Boosting Fenton-like reactions via single atom Fe catalysis, *Environ. Sci. Technol.* 53 (2019) 11391–11400.
- [5] L.J. Xu, J.L. Wang, Magnetic nanoscaled  $\text{Fe}_3\text{O}_4/\text{CeO}_2$  composite as an efficient Fenton-like heterogeneous catalyst for degradation of 4-chlorophenol, *Environ. Sci. Technol.* 46 (2012) 10145–10153.
- [6] C. Dai, X. Tian, Y. Nie, H.M. Lin, C. Yang, B. Han, Y. Wang, Surface facet of  $\text{CuFe}_2\text{O}_4$  nanocatalyst: a key parameter for  $\text{H}_2\text{O}_2$  activation in Fenton-like reaction and organic pollutant degradation, *Environ. Sci. Technol.* 52 (2018) 6518–6525.
- [7] H. Xia, Z. Zhang, J. Liu, Y. Deng, D. Zhang, P. Du, S. Zhang, X. Lu, Novel Fe-Mn-O nanosheets/wood carbon hybrid with tunable surface properties as a superior catalyst for Fenton-like oxidation, *Appl. Catal. B Environ.* 259 (2019), 118058.
- [8] Y. Chen, C.J. Miller, T.D. Waite, pH Dependence of hydroxyl radical, ferryl, and/or ferric peroxo species generation in the heterogeneous Fenton process, *Environ. Sci. Technol.* 56 (2022) 1278–1288.
- [9] Y. Zhu, R. Zhu, Y. Xi, J. Zhu, G. Zhu, H. He, Strategies for enhancing the heterogeneous Fenton catalytic reactivity: a review, *Appl. Catal. B Environ.* 255 (2019), 117739.
- [10] Q. Chen, F. Lü, H. Zhang, P. He, Where should Fenton go for the degradation of refractory organic contaminants in wastewater? *Water Res.* 229 (2023), 119479.
- [11] Z. Ye, J.A. Padilla, E. Xuriguera, J.L. Beltran, F. Alcaide, E. Brillas, I. Sires, A highly stable metal-organic framework-engineered  $\text{Fe}_2\text{S}_2/\text{C}$  nanocatalyst for heterogeneous electro-Fenton treatment: validation in wastewater at mild pH, *Environ. Sci. Technol.* 54 (2020) 4664–4674.
- [12] J.J. Conde, S. Abelleira, S. Estevez, J. Gonzalez-Rodriguez, G. Feijoo, M.T. Moreira, Improving the sustainability of heterogeneous Fenton-based methods for micropollutant abatement by electrochemical coupling, *J. Environ. Manag.* 332 (2023), 117308.
- [13] N. Wang, Q. Hu, X. Du, H. Xu, L. Hao, Study on decolorization of Rhodamine B by raw coal fly ash catalyzed Fenton-like process under microwave irradiation, *Adv. Powder Technol.* 30 (2019) 2369–2378.
- [14] S. Zhang, T. Hedtko, X. Zhou, M. Elimelech, J.H. Kim, Environmental applications of engineered materials with nanoconfinement, *ACS ES&T Eng.* 1 (2021) 706–724.
- [15] L. Wang, Z. Wang, S.K. Patel, S. Lin, M. Elimelech, Nanopore-based power generation from salinity gradient: why it is not viable, *ACS Nano* 15 (2021) 4093–4107.
- [16] E.G. Kovaleva, L.S. Molochnikov, U. Venkatesan, A. Marek, D.P. Stepanova, K. V. Kozhikhova, M.A. Mironov, A.I. Smirnov, Acid-base properties of nanoconfined volumes of anodic aluminum oxide pores by EPR of pH-sensitive spin probes, *J. Phys. Chem. C* 120 (2016) 2703–2711.
- [17] J. Wordsworth, T.M. Benedetti, A. Alinezhad, R.D. Tilley, M.A. Edwards, W. Schuhmann, J.J. Gooding, The importance of nanoscale confinement to electrocatalytic performance, *Chem. Sci.* 11 (2020) 1233–1240.
- [18] A. Nouri-Khorasani, K. Malek, A. Malek, T. Mashio, D.P. Wilkinson, M.H. Eikerling, Molecular modeling of the proton density distribution in a water-filled slab-like nanopore bounded by Pt oxide and ionomer, *Catal. Today* 262 (2016) 133–140.
- [19] M. Zhao, Y. Liu, B. Su, Anomalous proton transport across silica nanochannel membranes investigated by ion conductance measurements, *Anal. Chem.* 91 (2019) 13433–13438.
- [20] S. Zhang, T. Hedtko, L. Wang, X.X. Wang, T.C. Cao, M. Elimelech, J.H. Kim, Engineered nanoconfinement accelerating spontaneous manganese-catalyzed degradation of organic contaminants, *Environ. Sci. Technol.* 55 (2021) 16708–16715.
- [21] S. Zhang, M. Sun, T. Hedtko, A. Deshmukh, X. Zhou, S. Weon, M. Elimelech, J. H. Kim, Mechanism of heterogeneous Fenton reaction kinetics enhancement under nanoscale spatial confinement, *Environ. Sci. Technol.* 54 (2020) 10868–10875.
- [22] Y. Chen, G. Zhang, H.J. Liu, J.H. Qu, Confining free radicals in close vicinity to contaminants enables ultrafast Fenton-like processes in the interspacing of  $\text{MoS}_2$  membranes, *Angew. Chem. Int. Ed.* 58 (2019) 8134–8138.
- [23] H. Yi, E. Almatrafi, D.S. Ma, X.Q. Huo, L. Qin, L. Li, X.R. Zhou, C.Y. Zhou, G. M. Zeng, C. Lai, Spatial confinement: a green pathway to promote the oxidation processes for organic pollutants removal from water, *Water Res.* 233 (2023), 119719.
- [24] J. Weiss, C.W. Humphrey, Reaction between hydrogen peroxide and iron salts, *Nature* 163 (1949) 691.
- [25] J.R. Peller, S.P. Mezyk, W.J. Cooper, Bisphenol A reactions with hydroxyl radicals: diverse pathways determined between deionized water and tertiary treated wastewater solutions, *Res. Chem. Intermediat.* 35 (2009) 21–34.
- [26] X.X. Ji, H.F. Wang, P.J. Hu, First principles study of Fenton reaction catalyzed by  $\text{FeOCl}$ : reaction mechanism and location of active site, *Rare Met.* 38 (2019) 783–792.
- [27] I. Jarrige, Y.Q. Cai, S.R. Shieh, H. Ishii, N. Hiraoka, S. Karna, W.H. Li, Charge transfer in  $\text{FeOCl}$  intercalation compounds and its pressure dependence: an x-ray spectroscopic study, *Phys. Rev. B* 82 (2010), 165121.



- [28] E. Finkelstein, G.M. Rosen, E.J. Rauckman, Spin trapping. Kinetics of the reaction of superoxide and hydroxyl radicals with nitrones, *J. Am. Chem. Soc.* 102 (1980) 4994–4999.
- [29] S.E. Page, W.A. Arnold, K. McNeill, Terephthalate as a probe for photochemically generated hydroxyl radical, *J. Environ. Monit.* 12 (2010) 1658–1665.
- [30] G.V. Buxton, C.L. Greenstock, W.P. Helman, A.B. Ross, Critical review of rate constants for reactions of hydrated electrons, hydrogen atoms and hydroxyl radicals ( $\bullet\text{OH}/\bullet\text{O}^\cdot$ ) in aqueous solution, *J. Phys. Chem. Ref. Data* 17 (1988) 513–886.
- [31] J.A. LaVerne, The production of OH radicals in the radiolysis of water with  $^4\text{He}$  ions, *Radiat. Res.* 118 (1989) 201–210.
- [32] L. Han, S.G. Liu, J.Y. Liang, Y.J. Ju, N.B. Li, H.Q. Luo, pH-mediated reversible fluorescence nanoswitch based on inner filter effect induced fluorescence quenching for selective and visual detection of 4-nitrophenol, *J. Hazard. Mater.* 362 (2019) 45–52.
- [33] B. Baruah, G.J. Gabriel, M.J. Akbashev, M.E. Booher, Facile synthesis of silver nanoparticles stabilized by cationic polynorbornenes and their catalytic activity in 4-nitrophenol reduction, *Langmuir* 29 (2013) 4225–4234.
- [34] G. Guo, Q. Zheng, T. Li, T. Zhang, S. Tang, L. Li, S. Gao, Y. Tang, D. Chen, 3D printed self-calibrating on-site sensing platform based on bimodal excitation carbon dots for visual 4-nitrophenol detection by means of the localization of inner filter effect and pH regulation, *Chem. Eng. Sci.* 281 (2023), 119201.
- [35] E.G. Kovaleva, L.S. Molochnikov, D.O. Antonov, D.P.T. Stepanova, M. Hartmann, A.N. Tsmokalyuk, A. Marek, A.I. Smirnov, Proton activity in nanochannels revealed by electron paramagnetic resonance of ionizable nitroxides: a test of the Poisson–Boltzmann double layer theory, *J. Phys. Chem. C* 122 (2018) 20527–20538.
- [36] G. Bruno, N. Di Trani, R.L. Hood, E. Zabre, C.S. Filgueira, G. Canavese, P. Jain, Z. Smith, D. Demarchi, S. Hosali, A. Pimpinelli, M. Ferrari, A. Grattoni, Unexpected behaviors in molecular transport through size-controlled nanochannels down to the ultra-nanoscale, *Nat. Commun.* 9 (2018) 1682.
- [37] Y.H. Zhang, Y. Wang, Y. Li, Z.X. Xu, H.Z. Li, W. Jin, Reactivity of dissolved effluent organic matter (EfOM) with hydroxyl radical as a function of its isolated fractions during ozonation of municipal secondary effluent, *Water Res.* 242 (2023), 120248.
- [38] U. von Gunten, Ozonation of drinking water: part I. Oxidation kinetics and product formation, *Water Res.* 37 (2003) 1443–1467.